4-10-2013

Universal scaling and intrinsic classification of electro-mechanical actuators

Sambit Palit
Purdue University, spalit@purdue.edu

Ankit Jain
jankit@purdue.edu

Muhammad A. Alam
Purdue University, alam@purdue.edu

Journal of Applied Physics

Universal scaling and intrinsic classification of electro-mechanical actuators

Sambit Palit, Ankit Jain, and Muhammad Ashraful Alam

Citation: J. Appl. Phys. **113**, 144906 (2013); doi: 10.1063/1.4798365
View online: http://dx.doi.org/10.1063/1.4798365
View Table of Contents: http://jap.aip.org/resource/1/JAPIAU/v113/i14
Published by the American Institute of Physics.

JOURNAL OF APPLIED PHYSICS **113**, 144906 (2013)

Universal scaling and intrinsic classification of electro-mechanical actuators

Sambit Palit,[a] Ankit Jain,[a] and Muhammad Ashraful Alam[b]
School of Electrical and Computer Engineering, Purdue University, 465 Northwestern Avenue, West Lafayette, Indiana 47907, USA

(Received 7 February 2013; accepted 12 March 2013; published online 11 April 2013)

Actuation characteristics of electromechanical (EM) actuators have traditionally been studied for a few specific regular electrode geometries and support (anchor) configurations. The ability to predict actuation characteristics of electrodes of arbitrary geometries and complex support configurations relevant for broad range of applications in switching, displays, and varactors, however, remains an open problem. In this article, we provide four universal scaling relationships for EM actuation characteristics that depend only on the mechanical support configuration and the corresponding electrode geometries, but are independent of the specific geometrical dimensions and material properties of these actuators. These scaling relationships offer an intrinsic classification for actuation behavior of a broad range of EM actuators with vastly different electrode/support geometries. Consequently, the problem of analysis/design of complex EM actuators is reduced to the problem of determining only five scaling parameters, which can be obtained from no more than three independent characterization experiments or numerical simulations. © *2013 American Institute of Physics*. [http://dx.doi.org/10.1063/1.4798365]

I. INTRODUCTION

Electro-Mechanical (EM) actuators have diverse applications in varying fields both as an analog (tunable) and a digital (switch) element.[1] Analog applications involve continuous position control of a movable electrode, e.g., micro-mirrors for projectors,[2] external cavity tunable lasers,[3] reflective diffraction grating,[4] deformable mirrors for adaptive optics,[5] RF-MEMS varactors,[6] etc. On the other hand, digital operation requires only a binary position control of the movable electrode, e.g., RF-MEMS capacitive/ohmic switches,[7,8] NEMS relays,[9] interferrometric Mirasol displays,[10] etc. Fig. 1(a) depicts the schematic of a generic actuator where a movable electrode M_1 is suspended in air above a fixed bottom electrode M_2. The position and shape of M_1 is controlled by an external voltage source that creates an electric field and exerts a downward electrostatic force on M_1. The governing equation for the deflection z of M_1 with Young's modulus E, Poisson's ratio ν, thickness H, and subjected to an externally applied potential V is given by

$$\frac{EH^3}{12(1-\nu^2)}\nabla_r^4 z = -\frac{1}{2}\frac{dC(r,z)}{dz}V^2, \tag{1}$$

where r is a vector in the plane of M_1 and $C(r,z)$ is the capacitance per unit area between M_1 and M_2 at position r. With the increase in the applied voltage V, M_1 bends down to balance the increase in electrostatic force by an equal and opposite elastic restoring force. Beyond the *pull-in voltage* (V_{PI}), the electrostatic force exceeds the restoring force, and M_1 snaps down to come in contact with a thin dielectric deposited over M_2. When the voltage drops below the *pull-out voltage* (V_{PO}), the electrostatic force fails to overcome the elastic restoring force and M_1 springs back in the air. This operation is hysteretic with two inherent instabilities, namely, *pull-in* (PI) and *pull-out* (PO), demonstrated using a simulated Capacitance (C)–Voltage (V) characteristic in Fig. 1(b). There are two modes of operation of the actuator—(i) when M_1 is in air (*below pull-in* state) and (ii) when M_1 is in contact with the dielectric on the bottom electrode (*post pull-in* state). The actuator is operated in the *below pull-in* state for analog applications and switched between *below pull-in* and *post pull-in* states for digital applications. The dynamics of an actuator is fundamentally governed by the geometry and support configurations of the electrodes (see Fig. 1(c) for various examples). Note that residual stress and mid-plane stretching[11,12] have been neglected in Eq. (1).

Since Taylor's pioneering experiments with charged soap-bubbles (to explore the physics behind thunderstorm formation[13]) and the invention of the first microactuator a few years later (resonant gate transistor[14]), electrode geometries and support configurations in actuators have evolved significantly. Electrode geometry has changed from being planar (graphene electrodes[15]), to cylindrical (suspended carbon nanotubes (CNT)[16] and silicon nanowires[17]), and to an array of cylinders (nanowire arrays[18]). Similarly, the support configuration has changed from fixed-fixed and fixed-free (cantilever), to circular (clamped on all sides), and to serpentine coils.[19] Likewise, the design of commercially available switches[20] have evolved to either having patterned dielectrics on the bottom electrode (M_2) and/or holes in the top electrode (M_1) to improve reliability and/or performance of the actuator.[21]

With such a broad variance in the electrode geometries and support configurations, analysis of actuation characteristics is often done on a *case-by-case* basis. There is vast literature on planar[11,22] and cylindrical electrode[16,23] geometries, and analytical solutions for idealized regular support configurations (e.g., fixed-fixed,[24] cantilever,[25] and circular[26]) are

[a]S. Palit and A. Jain contributed equally to this work.
[b]Email: alam@purdue.edu

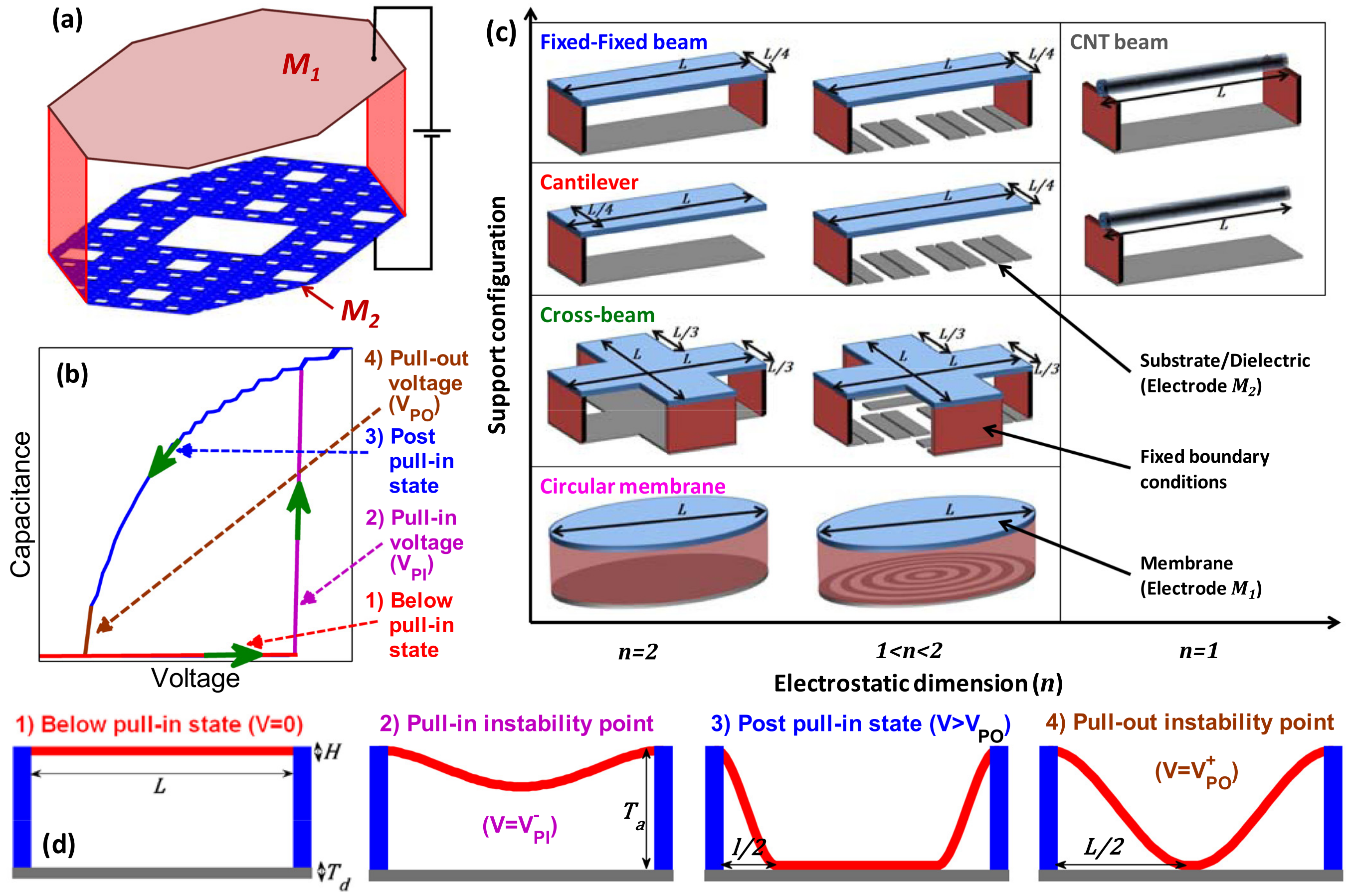

FIG. 1. (a) Schematic of a generic EM actuator with electrode M_1 having arbitrary geometry and support configurations and a (fractal) patterned bottom electrode M_2. (b) Typical hysteretic *C-V* characteristics with the four defining characteristics marked—(1) *Below pull-in* state ($0 \leq V < V_{PI}$), (2) *Pull-in voltage* ($V = V_{PI}$), (3) *Post pull-in* state ($V > V_{PO}$), and (4) *Pull-out voltage* ($V = V_{PO}$). (c) Geometry and support configurations of different *geometry-classes* being simulated to study scaling laws. The blue (horizontal) regions represent M_1 and the red (vertical) regions indicate a fixed support configuration. The gray (horizontal) regions represent M_2. Voltage is applied between M_1 and M_2. The various *geometry-classes* are classified according to the electrostatic dimension of the system (n) and the support configuration. Note that the carbon nanotube (CNT) can be subjected to either a fixed-fixed or a cantilever support configuration. (d) Typical shapes of M_1 at $V = 0$, at pull-in instability point ($V = V^-_{PI}$), *post pull-in* state ($V > V_{PO}$), and at pull-out instability point ($V = V^+_{PO}$) for fixed-fixed support configuration.

known. There is, however, no general framework to analyze EM actuators having arbitrary electrode geometries and support configurations. Lack of such a theoretical framework impedes the optimal design of electrode geometry towards achieving desired performance or comparing the response of closely related actuators. Even though the pull-in behavior of the actuators has already been analyzed in depth,[27] the understanding of pull-out actuation and the *post pull-in* configurations remain far more elementary. And yet, it is the pull-out actuation that defines (stiction-related) failure times of RF-MEMS capacitive switches caused by dielectric charging.[28–31]

In this paper, we provide scaling relationships for four aspects of the actuation behavior: (a) *pull-in voltage* (V_{PI}), (b) C_{bp}-V response in *below pull-in* (BP) state, (c) *pull-out voltage* (V_{PO}), and (d) C_{pp}-V response in *post pull-in* (PP) state. The scaling relationships are shown to be universal across a wide range of geometries, support configurations, and patterned bottom electrodes. These scaling relationships can not only be used to interpret actuation characteristics of a given device, but also be used to optimize actuator geometries for obtaining desired performance.

II. SCALING RELATIONSHIPS

To unify actuation characteristics, we introduce the concept of a *geometry-class* (GC). All actuators belonging to the same GC share the same electrode geometries, support configurations, and patterning. We analyze four generic support configurations in this work: fixed-fixed (e.g., capacitive RF-MEMS switches[20]), cantilevers (e.g., ohmic switches[32]), cross shaped (e.g., air-flow sensors[33]), and circular (e.g., pressure sensors[34]). We also include two additional cases where (i) M_1 is cylindrical (e.g., CNT based NEMS[16]) and (ii) M_2 is patterned as a fractal. The GCs analyzed in this work are summarized in Fig. 1(c).

We consider a two-dimensional actuator system, where M_1 is described by a single length dimension (L). We assume a general expression for capacitance per unit area given by $C(z) = \frac{\epsilon_0 \beta L^{n-2}}{(z+T_d)^{n-1}}$, where n is a parameter (named *electrostatic dimension*) that defines the electrostatics of the system, and is fundamentally related to the geometry of M_1 and patterning on M_2. Equation (1), therefore, reduces to

$$D\frac{d^4 z}{dx^4} = -\frac{1}{2}\frac{dC(z)}{dz}V^2 = \frac{n-1}{2}\frac{\epsilon_0 \beta L^{n-2}}{(z+T_d)^n}V^2, \qquad (2)$$

where $D \equiv \frac{EH^3}{12(1-\nu^2)}$ is the flexural rigidity of M_1, ϵ_0 is the permittivity of free space, T_d is the effective dielectric thickness normalized by the dielectric constant ϵ_r, L is the length-scale of M_1, and β is a constant that depends exclusively on the geometrical configuration of the electrodes: e.g., classical planar electrodes are defined by $\beta = 1$ and $n = 2$. It is known that the capacitance of fractal electrodes can likewise be described by the exponent n ($\cong D_F$, the fractal dimension), and a constant β that depends exclusively on D_F (see Ref. 35 and Sec. 2 of Ref. 36).

We scale z and x by the scaling lengths z_0 and l, respectively, such that $\tilde{z} = \frac{z+T_d}{z_0}$ and $\tilde{x} = \frac{x}{l}$. Here, $z_0 = T_a + T_d$ is the effective air-gap (T_a being the physical air-gap) and l is the length of the part of M_1 suspended in air, see Fig. 1(d). Note that while $l = L$ for device operation in the BP state, $l \leq L$ after the top electrode has been pulled-in (PP state). We derive the following scaling laws (detailed derivation given in Appendix A), which unifies actuation and C-V behavior of actuators across all GCs independent of material properties and physical dimensions-

$$\text{Pull-in voltage:} \quad V_{PI} = \alpha_{PI}\sqrt{\frac{K_0 z_0^2}{(n-1)C_{OFF}}} = \alpha_{PI} V_0, \quad (3)$$

$$C_{bp} - V\,\text{characteristic:} \quad \frac{C_{bp}}{C_{OFF}} = \tilde{f}\left(\frac{V}{V_{PI}}\right), \quad (4)$$

$$\text{Pull-out voltage:} \quad V_{PO} = \alpha_{PO}\sqrt{\frac{K_0 z_0^2}{(n-1)C_{ON}}\left(\frac{z_0}{T_d}\right)^{\gamma}} = \alpha_{PO} V_1, \quad (5)$$

$$C_{pp}\text{-}V\ \text{characteristic:} \quad \frac{C_{ON} - C_{PO}}{C_{ON} - C_{pp}} = \left(\frac{V}{V_{PO}}\right)^{\kappa}. \quad (6)$$

Here, $K_0 \equiv \frac{EH^3}{6(1-\nu^2)L^3}$ is related to the effective *stiffness* of the top electrode (M_1), $C_{OFF} \equiv \frac{\epsilon_0 \beta L^{n-1}}{z_0^{n-1}}$ is the off-state capacitance per unit width, C_{bp} is the capacitance in the BP state, $C_{ON} \equiv \frac{\epsilon_0 \beta L^{n-1}}{T_d^{n-1}}$ is the maximum attainable on-state capacitance, C_{PO} is the capacitance at the PO instability point, and C_{pp} is the capacitance in the PP state. The scaling variables α_{PI} (*pull-in coefficient*), α_{PO} (*pull-out coefficient*), γ (*geometry-exponent*), κ (*scaling-exponent*), and the function $\tilde{f}$ depend exclusively on the GC of the actuator.

Equations (3)–(6) define the core set of universal scaling relationships for electro-mechanical actuation for all GCs, characterized by only five scaling parameters—α_{PI}, α_{PO}, γ, κ, and the function $\tilde{f}$. We observe that, in practice, $\gamma \approx 1$ and $\kappa \approx 0.5$ for all GCs, so that only the remaining three scaling parameters (i.e., α_{PI}, α_{PO}, and the function $\tilde{f}$) need to be determined in order to predict the actuator response to a good approximation. Additionally, the scaling function $\tilde{f}$ can be decomposed into a scaling parameter δ and an analytically known function $\tilde{f}_A$, as discussed in Appendix B. Although the normalized Eq. (3) is well known and the scaling solution for pull-in characteristics (Eqs. (3) and (4)) have been verified in isolated contexts for regularized geometry, the behavior of the pull-in and pull-out actuation voltages and capacitances response for a full range of arbitrary electrode geometries (characterized by n and β) and support configurations have never been explored. The generalization and unification of EM actuation characteristics using the scaling results are the key contribution of this work.

III. VERIFICATION OF SCALING LAWS

We verify the scaling relationships for V_{PI}, C_{bp}, V_{PO}, and C_{pp} given by Eqs. (3)–(6), respectively, for the various GCs shown schematically in Fig. 1(c). For numerical validation, the deflected shapes of M_1 are calculated using Kirchoff-Love (KL) plate equation[37] and the downward electrostatic force is determined by solving Poisson equation using Method of Moments (MOM) (see supplementary material[36] Sec. 1 for details). Note that the solution obtained using MOM ensures that the electrostatic force includes full 3D fringing field effects. For a comprehensive and statistically robust verification of the scaling relationships, we simulate C-V characteristics of 100 randomly configured actuators for each GC, with varying L, H, T_a, T_d, ϵ_r, E, and ν. The actuation voltages V_{PI} and V_{PO} as well as C_{bp}-V and C_{pp}-V responses are determined from the numerically simulated C-V characteristics. As we see in Fig. 2(a), the actuation voltages vary within a wide range of 0.5 V–50 V (due to the variance in geometrical configurations and material properties). These numerically calculated values are then used with the scaling relationships discussed in Sec. II to determine the scaling parameters associated with specific GCs.

A. Scaling for regular electrodes

In Fig. 2(a), we plot $\log(V_{PI})$ against $\log(V_0)$ for all the 100 devices simulated for each of the four support configurations with regular bottom electrodes ($n = 2$; 1st column in Fig. 1(c)) and the CNT beam in fixed-fixed support configuration (3rd column in Fig. 1(c)), to verify V_{PI} scaling relationship described in Eq. (3). We observe that the simulated data-points lie on a straight line with a slope of 1, consistent with Eq. (3). The intercepts of the straight line is equal to $\log(\alpha_{PI})$. Remarkably, α_{PI} depends only on the GC and not on specific physical dimensions and material properties. Physically, we expect α_{PI} to increase with more restrictive support configurations (i.e., cantilever, fixed-fixed, cross-shaped, circular in increasing order)—this hypothesis is generally supported by the results in Fig. 2(a). Similarly, Fig. 2(b) shows that $\frac{C_{bp}}{C_{OFF}}$ in the BP state has the same functional dependence (defined by the scaling function $\tilde{f}$) on $\frac{V}{V_{PI}}$, irrespective of the actuator dimensions and material properties for each of the five cases considered. This result was anticipated by Eq. (4).

The process of verification of scaling relationships for V_{PO} and PP C-V characteristics (and consequently the determination of the scaling variables α_{PO}, γ, and κ) in Eqs. (5) and (6) follows a similar procedure as described in the previous paragraph. To determine γ (Eq. (5)), an intermediate step is involved, where the value of γ associated with a particular GC is defined by the slope of a straight line fit of the plot of $\log(A)$ against $\log(B)$ (where $A \equiv \frac{V_{PO}^2(n-1)C_{ON}}{K_0 z_0^2}$ and $B \equiv \frac{z_0 \epsilon_r}{T_d}$; see Fig. 2(c)). Our results show that $\gamma \approx 1$ across the different

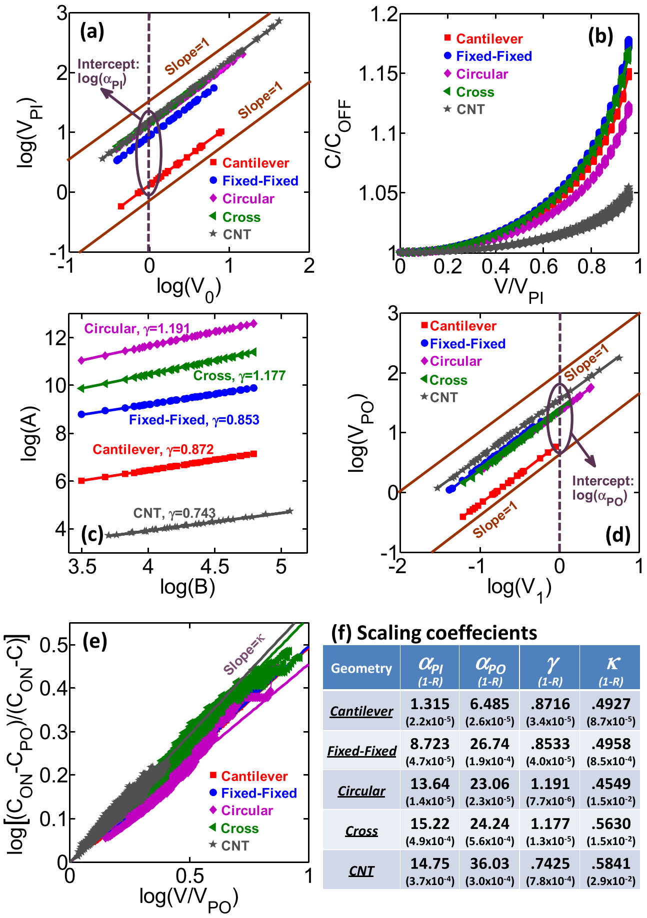

Geometry	α_{PI} (1-R)	α_{PO} (1-R)	γ (1-R)	κ (1-R)
Cantilever	1.315 (2.2×10^{-5})	6.485 (2.6×10^{-5})	.8716 (3.4×10^{-5})	.4927 (8.7×10^{-5})
Fixed-Fixed	8.723 (4.7×10^{-5})	26.74 (1.9×10^{-4})	.8533 (4.0×10^{-5})	.4958 (8.5×10^{-4})
Circular	13.64 (1.4×10^{-5})	23.06 (2.3×10^{-5})	1.191 (7.7×10^{-6})	.4549 (1.5×10^{-2})
Cross	15.22 (4.9×10^{-4})	24.24 (5.6×10^{-4})	1.177 (1.3×10^{-5})	.5630 (1.5×10^{-2})
CNT	14.75 (3.7×10^{-4})	36.03 (3.0×10^{-4})	.7425 (7.8×10^{-4})	.5841 (2.9×10^{-2})

FIG. 2. Verification of the scaling laws in Eqs. (3)–(6), with simulation results from 100 randomly configured actuators. (a) Plot of $\log(V_{PI})$ vs. $\log(V_0)$ to verify Eq. (3), and extraction of α_{PI}. (b) Plot of C_{bp}/C_{OFF} vs. V/V_{PI}, verifying Eq. (4) and determination of $\tilde{f}$. (c) Extraction of γ. (d) Plot of $\log(V_{PO})$ vs. $\log(V_1)$ to verify Eq. (5) and extraction of α_{PO}. (e) Verification of C_{pp} scaling law in Eq. (6) and extraction of κ. (f) A table summarizing the values obtained for α_{PI}, α_{PO}, γ, and κ for the five GCs considered for this figure, with correlation coefficients (R) of the fits.

GCs for a planar bottom electrode, but is somewhat lower for CNT ($\gamma \sim 0.743$). Using this value of γ, we plot $\log(V_{PO})$ against $\log(V_1)$ for all the simulated actuators from the different GCs (Fig. 2(d)). Similar to Fig. 2(a) for V_{PI} scaling, we find that PO behavior also scales in accordance with a GC dependent coefficient α_{PO}, therefore verifying the V_{PO} scaling law (Eq. (5)). Note that α_{PO} is also dependent on the restrictiveness of the support configurations. Finally, we verify scaling of the PP C-V characteristics described by Eq. (6) in Fig. 2(e), where the line indicates a linear dependence on $\left(\frac{V}{V_{PO}}\right)^{\kappa}$, with $\kappa \approx 0.5$. Note that there is a spread in the observed value of κ because of an implicit approximation used to derive Eq. (6); however, the value of $\kappa \approx 0.5$ can still be justified (see Appendix C).

The table in Fig. 2(f) summarizes the values of α_{PI}, α_{PO}, γ, and κ obtained for the five GCs thus considered. Note that for the CNT beam, even though the functional dependence of $C(z)$ is somewhat different from the one used in Eq. (2),[16] the scaling laws hold reasonably well for this case as well. This indicates the universality of the scaling relations in Eqs. (3)–(6). Unlike PI actuation and BP operation, PO actuation and PP operation are associated with three GC dependent scaling parameters—α_{PO}, γ, and κ. Even if one approximates $\gamma \approx 1$ and $\kappa \approx 0.5$, so as to work with single scaling parameter α_{PO}, we find that the theory estimates V_{PO} to within 30% across all GCs. The estimates improve significantly if the scaling parameters are determined independently from experiments, as will be discussed later.

B. Scaling for fractal electrodes

So far we have discussed and verified scaling laws for top electrodes having arbitrary geometries and support configurations, with the bottom electrode being assumed as planar. The bottom electrode and the dielectric are frequently patterned to reduce charge injection in the dielectric and to improve reliability.[20] Here, we show that as long as the patterned electrodes can be approximated as a fractal (e.g., fractal electrodes for electrochemical applications,[38] and fractal antennas[39]), the scaling relationships (verified for regular planar electrodes) hold. The capacitance $C(z)$ for fractal electrodes follows a similar relationship as planar electrodes (Eq. (2)), but with an electrostatic dimension n ($\cong D_F$, the fractal dimension of the bottom electrode) and a fractal geometry dependent factor β. This $C(n)$-D_F relationship was verified using MOM for fractal Cantor beams (see Sec. 2 of Ref. 36 for further details).

The verification of scaling laws for fractal electrodes ($1.2 \le D_F \le 2$) with various types of supports (2nd column in Fig. 1(c)) are summarized in Fig. 3. The methodology follows the approach used for regular electrodes as discussed earlier. Once again, the C-V characteristics of 100 randomly configured devices from each of the four GCs (with a specific n and D_F) are obtained by numerically solving Eq. (1) in three dimensions using MOM. The results confirm the validity of the scaling relationships anticipated by Eqs. (3)–(6) (see Figs. 3(a)–3(d) for the specific case of a fixed-fixed

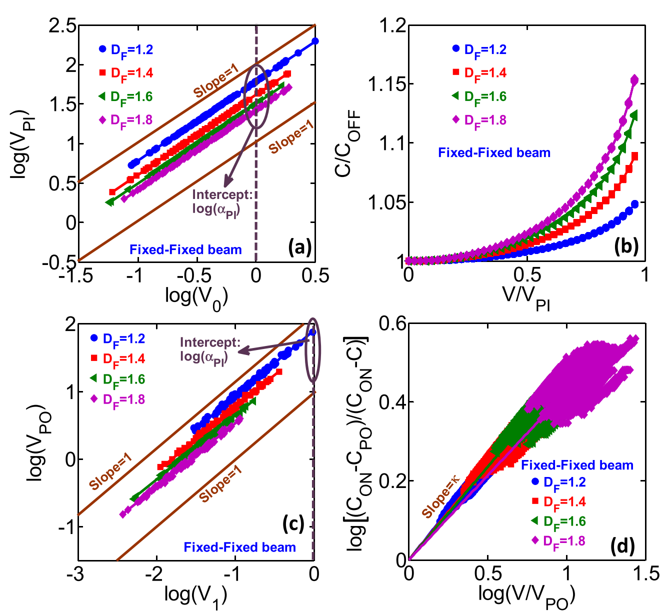

FIG. 3. Verification of scaling laws with simulation results from 100 randomly configured actuators with a fixed-fixed support configuration with fractal bottom electrode patterning. n is varied between 1.2 and 1.8. Plots of (a) $\log(V_{PI})$ vs. $\log(V_0)$ (b) C_{bp}/C_{OFF} vs. V/V_{PI}, and (c) $\log(V_{PO})$ vs. $\log(V_1)$ to verify Eqs. (3)–(5), respectively. (d) Verification of C_{pp} scaling law in Eq. (6).

support configuration). Similar results are obtained for other types of supports as well (see Sec. 3 of Ref. 36 for further details). The value of the scaling exponent κ is found to lie between 0.4 and 0.6 for all actuator geometries, support configurations, and electrostatic dimensions due to patterned bottom electrode.

IV. CHARACTERIZATION OF SCALING PARAMETERS

The scaling relationships in Eqs. (3)–(6) help reduce the problem of designing new EM actuators to determining the corresponding scaling parameters from either a few ($\sim$2–3) characterization experiments or FEM (Finite Element Method) simulations. Given these scaling parameters, one can determine geometric parameters that would produce targeted values of V_{PI}, V_{PO}, C_{bp}, and C_{pp}.

Specifically, one can use a *single* C-V measurement or a numerical FEM simulation of the target system (associated with a given *geometry-class*) to determine V_{PI} and C_{bp}-V characteristics. Since V_0 for the test device is known (based on physical dimensions and material properties), α_{PI} and $\tilde{f}$ are obtained using Eqs. (3) and (4), respectively. Similarly, one can determine the remaining three scaling parameters using Eqs. (5) and (6). Independent measurements (or simulations) of C_{pp}-V of two actuators (from the same GC) having different values of T_a, T_d, or ϵ_r are sufficient to calculate the value of γ, and subsequently scaling variables α_{PO} and κ.

Once the five scaling parameters (α_{PI}, γ, α_{PO}, κ, and function $\tilde{f}$) are known based on characterization or simulation data from two actuators of the same GC, the scaling relationships will specify the actuation voltages (V_{PI} and V_{PO}), as well as the C_{bp}-V and C_{pp}-V responses of any actuator from the same GC.

V. CONCLUSIONS

To summarize, we have developed four fundamental scaling relationships for key performance metrics of electromechanical actuators, which are independent of the geometry and support configurations imposed on the top actuating electrode, and patterning on the bottom electrode. These scaling laws dictate how the actuation voltages (Eq. (3) for V_{PI} and Eq. (4) for V_{PO}) and the C-V response during both *below pull-in* (Eq. (5)) and *post pull-in* (Eq. (6)) operation scale with device dimensions and material parameters. Apart from providing a theoretical justification behind the existence of these scaling laws, we have verified them numerically using the Kirchhoff-Love plate theory for deflected electrode shapes, and the Method-of-Moments to solve for electrostatic force. This unified framework of scaling relationships offers new insights regarding the role of beam-mechanics and electrostatic actuation in determining the performance of electromechanical actuators and allows an intrinsic geometry independent classification of all electromechanical actuators.

ACKNOWLEDGMENTS

The authors gratefully acknowledge NNSA-PRISM (#DE-FC52-08NA28617) and MIT-MSD (# 5710002706) centers for funding and support and Network for Computational Nanotechnology (NCN-#0634750-EEC) for providing the computational resources.

APPENDIX A: DERIVATION OF SCALING RELATIONSHIPS

After scaling z and x by scaling lengths z_0 and l, Eq. (2) therefore transforms to

$$\tilde{z}^n \frac{d^4\tilde{z}}{d\tilde{x}^4} = -\left(\frac{l}{L}\right)^4 \left(\frac{V}{V_0}\right)^2, \tag{A1}$$

where $V_0^2 \equiv \frac{2Dz_0^{n+1}}{(n-1)\epsilon_0 \beta L^{n+2}}$ is a constant that depends purely on the geometry and material properties of actuator. For the special case of $n=2$ (classical planar electrodes), Eq. (A1) reduces to a well-known form that has been studied by many groups.[24,25]

In the BP state, $l = L$, hence Eq. (A1) suggests that $\tilde{z}$ depends exclusively on a single parameter $\frac{V}{V_0}$. This implies that although the value of V_0 for different actuators could vary significantly depending on varying length scales, air-gaps and material properties, the normalized beam-shape of all actuators at the pull-in instability point must be identical. As a confirmation of this assertion, we see in Figs. 4(a) and 4(b) that the (numerically calculated) beam shapes overlap perfectly in the normalized dimensions $\tilde{x}$ and $\tilde{z}$ at the point of pull-in instability. The pull-in voltage, V_{PI}; therefore, should be a constant multiple of V_0, i.e.,

$$V_{PI} = \alpha_{PI} V_0 = \alpha_{PI}\sqrt{\frac{K_0 z_0^2}{(n-1)C_{OFF}}}, \tag{A2}$$

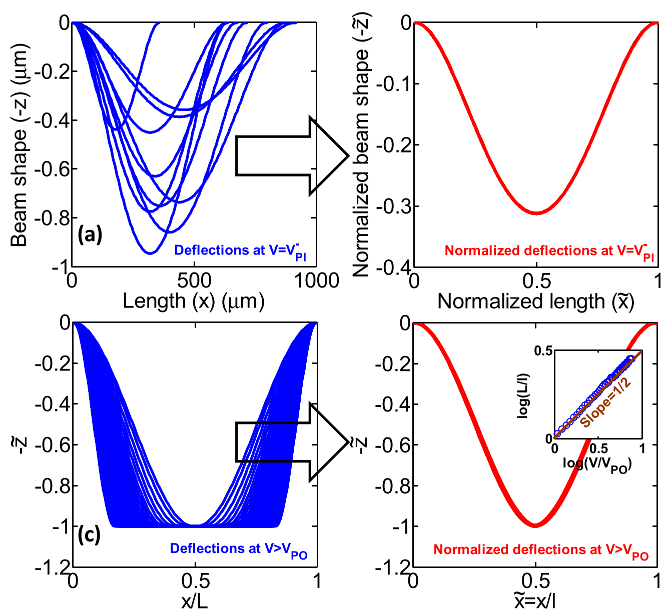

FIG. 4. Basis for scaling relationships in the case of a fixed-fixed support configuration. (a) Top electrode shapes for 10 randomly sized fixed-fixed actuators at the point of pull-in instability ($V = V_{PI}^-$). (b) The beam shapes in (a) overlap perfectly in normalized dimensions $\tilde{x}$ and $\tilde{z}$. (c) Beam shapes for a single fixed-fixed actuator during the post pull-in state. (d) The beam shapes in (c) overlap perfectly in normalized dimensions $\tilde{x}$ and $\tilde{z}$. Inset: Variation of the length of the non-contact part of the beam (l) with voltage (V) plotted to verify Eq. (6).

where $K_0 \equiv \frac{2D}{L^3}$ is related to the effective *stiffness* of the top electrode and $C_{OFF} \equiv \frac{\epsilon_0 \beta L^{n-1}}{z_0^{n-1}}$ is the off-state capacitance per unit width. Equation (3) is the same as Eq. (A2) above. The proportionality factor α_{PI} is the *pull-in coefficient* that depends entirely on the GC of the actuator, with actuator specific length scales and material properties being incorporated inside other terms.

Next, since capacitance per unit width is given by $C_w = \int_0^1 \frac{\epsilon_0 \beta L^{n-1}}{z_0^{n-1}\tilde{z}^{n-1}} d\tilde{x}$, it implies that $\frac{C_w}{C_{OFF}} = \int_0^1 \frac{1}{\tilde{z}^{n-1}} d\tilde{x}$, and therefore is a function dependent exclusively on $\frac{V}{V_0}$ as well. In other words, the capacitance in the BP state (C_{bp}) is given by

$$\frac{C_{bp}}{C_{OFF}} = f\left(\frac{V}{V_0}\right) = \tilde{f}\left(\frac{V}{V_{PI}}\right). \tag{A3}$$

The scaling function $\tilde{f}(\frac{V}{V_{PI}})$ depends on the GC. Equation (4) is the same as Eq. (A3) above. This function can be further approximated using a GC dependent scaling parameter δ and an analytical function $\tilde{f_A}$[40] derived for the case of a spring-mass system (see Appendix B for details).

After pull-in, only a part of M_1 is in contact with the dielectric over M_2. The remaining part of M_1 hangs in the air. Therefore, $l \leq L$. Remarkably, even after pull-in, the functional dependences of the scaled beam shapes ($\tilde{z}$) with respect to $\tilde{x}$ are the same and do not depend on the specific voltage (see Figs. 4(c) and 4(d)). This result, in combination with Eq. (A1), leads to[41]

$$l^4 V^2 \equiv L^4 V_{PO}^2 = L^4 V_0^2 \tilde{z}^n \frac{d^4\tilde{z}}{d\tilde{x}^4}, \tag{A4}$$

where V_{PO} is defined to be the voltage when $l = L$ (M_1 contacts M_2 only at a single point) in the PP state, implying that $(\tilde{x}, \tilde{z}) = (\frac{1}{2}, \frac{T_d}{z_0})$ at the point of PO instability. Therefore from Eq. (A4), $V_{PO}^2 = V_0^2 (\frac{T_d}{z_0})^n \frac{d^4\tilde{z}}{d\tilde{x}^4}$. Assuming that $\frac{d^4\tilde{z}}{d\tilde{x}^4} = \zeta(\frac{T_d}{z_0}) \propto (\frac{z_0}{T_d})^\eta$, where $\zeta(\frac{T_d}{z_0})$ indicates a function dependent on $\frac{T_d}{z_0}$ and η is an arbitrary GC dependent constant, the expression for V_{PO}^2 simplifies to $V_{PO}^2 = \frac{2D z_0^{n+1}}{(n-1)\epsilon_0 \beta L^{n+2}} (\frac{T_d}{z_0})^n (\frac{z_0}{T_d})^\eta$. Subsequently, we obtain

$$V_{PO} = \alpha_{PO} \sqrt{\frac{K_0 z_0^2}{(n-1)C_{ON}} \left(\frac{z_0}{T_d}\right)^\gamma} = \alpha_{PO} V_1. \tag{A5}$$

Here, $C_{ON} \equiv \frac{\epsilon_0 \beta L^{n-1}}{T_d^{n-1}}$ is the maximum attainable on-state capacitance, α_{PO} is the *pull-out coefficient*, and $\gamma \equiv \frac{\eta}{2} - 1$ is the *geometry-exponent*. Equation (5) is the same as Eq. (A5) above. The scaling parameters α_{PO} and γ can be determined, given V_{PO} is known for a *pair* of actuators, obtained either from experiments or from simulation results. Similar to α_{PI}, α_{PO} depends entirely on the GC of the actuator, with length scales and material properties being incorporated inside other terms in Eq. (A5).

The total capacitance during PP state (C_{pp}) has two components, from the parts of the M_1 which are either (i) suspended in air or (ii) in contact with the dielectric. Therefore, as an approximation,

$$C_{pp} \approx C_{ON} \frac{A_c}{A} + \frac{A_a}{A} C_{PO} = C_{ON} \frac{(A - A_a)}{A} + \frac{A_a}{A} C_{PO}, \tag{A6}$$

where C_{PO} is the capacitance at the point of pull-out instability, A is the total area of M_1, A_c is the area of M_1 in contact with the dielectric on M_2, and A_a is the area of M_1 suspended in air. Note that $A_c + A_a = A$. In case of fixed-fixed and fixed-free support configurations, we observe that $\frac{A}{A_a} = \frac{L}{l}$. Therefore, after simplifying Eq. (A6) and using Eq. (A4), we can obtain

$$\frac{C_{ON} - C_{PO}}{C_{ON} - C_{pp}} = \frac{A}{A_a} = \frac{L}{l} = \left(\frac{V}{V_{PO}}\right)^\kappa, \tag{A7}$$

where $\kappa \approx 0.5$ is the *scaling-exponent*; Eq. (6) is the same as Eq. (A7) above.

In practice, high precision numerical simulations suggest that $\kappa = 0.5 \pm 0.1$. The observed spread in κ reflects the implicit approximation in Eq. (A6). In case of a circular and cross shaped support configuration, the relation $\frac{A}{A_a} = \frac{L}{l}$ needs to be restated differently; however, the value of $\kappa \approx 0.5$ can still be justified (see Appendix C for details).

APPENDIX B: ANALYTICAL APPROXIMATION FOR C_{bp}-V RELATIONSHIP

The analytical expression of the scaled air-gap ($\tilde{z_A}$) as a function of $\frac{V}{V_{PI}}$ for a spring mass model has been analytically derived.[40] Consequently, one can derive the analytical expression for $(\frac{C_{bp}}{C_{OFF}})_A$ as a function of $\tilde{z_A}$ for a spring-mass system as follows:

$$\begin{aligned}\tilde{f_A}\left(\frac{V}{V_{PI}}\right) &= \left(\frac{C_{bp}}{C_{OFF}}\right)_A = \frac{1}{\tilde{z_A}} \\ &= \frac{3}{1 + 2\cos\left(\frac{1}{3}\cos^{-1}\left(1 - 2\left(\frac{V}{V_{PI}}\right)^2\right)\right)}.\end{aligned} \tag{B1}$$

We assume that the numerically obtained/experimentally characterized value of the change in C_{bp} is proportional to its analytical equivalent. In other words,

$$\frac{C_{bp} - C_{OFF}}{C_{OFF}} = \delta \times \left(\frac{C_{bp} - C_{OFF}}{C_{OFF}}\right)_A, \tag{B2}$$

where δ is a proportionality factor. Using Eq. (B2), scaling function $\tilde{f}$ can therefore be expressed as

$$\begin{aligned}\tilde{f}\left(\frac{V}{V_{PI}}\right) &= 1 + \frac{C_{bp} - C_{OFF}}{C_{OFF}} = 1 + \delta \times \left(\frac{C_{bp} - C_{OFF}}{C_{OFF}}\right)_A \\ &= 1 + \delta \times \left(\frac{1}{\tilde{z_A}} - 1\right) = 1 + \delta \times \left(\tilde{f_A}\left(\frac{V}{V_{PI}}\right) - 1\right).\end{aligned} \tag{B3}$$

Substituting the value of $\tilde{z_A}$ from Eq. (B1) in Eq. (B3), we can express the scaling function $\tilde{f}$ analytically, in terms of a single scaling parameter δ. This claim is tested by obtaining a best fit between numerically simulated and analytically obtained values for $\tilde{f}$ for five GCs, namely,

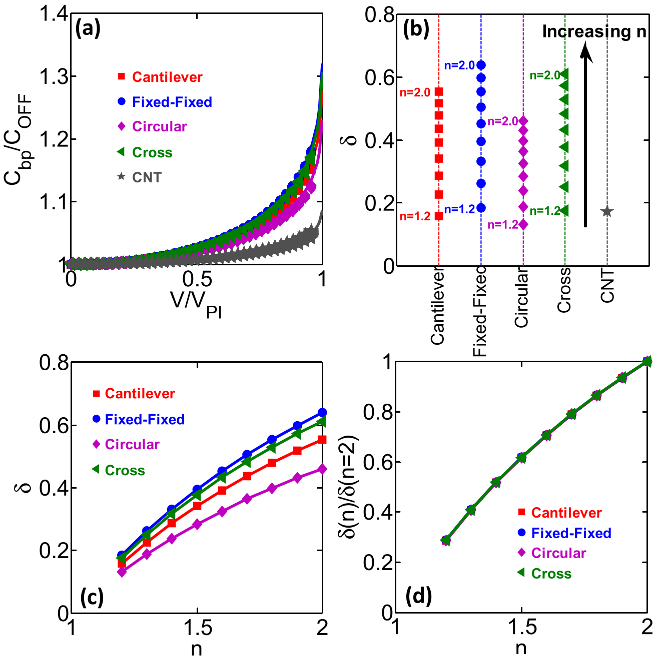

FIG. 5. Analytical approximation for the scaling function f into an analytically known function $\tilde{f}_A$ and a scaling parameter δ (Eq. (B3). (a) Comparison between numerically obtained function $\tilde{f}$ and Eq. (B3) using a best-fit value of δ for the four geometry-classes with regular bottom electrode (1st column in Fig. 1(c)) and a CNT electrode subjected to a fixed-fixed support configuration (3rd column in Fig. 1(c)). (b) and (c) Summary of the values of δ obtained across various support configurations and electrostatic dimensions (n) due to bottom electrode patterning. Note that the error bars obtained for δ are also drawn in (b), but are so small that they cannot be seen. (d) Plot of $\delta(n)/\delta(n=2)$ for all the four support configurations being studied. The normalized values of δ for the different support configurations overlap each other perfectly.

cantilever, fixed-fixed, circular membrane, and cross-beam of electrostatic dimension $n = 2$, and a CNT beam in Fig. 5(a). We observe that the analytical model with a best-fit δ is able to replicate the numerical results with excellent accuracy. In Figs. 5(b) and 5(c), we summarize the values of δ obtained for all the GCs studied in this work. The error bars of the fitting obtained for each data point (also plotted in Fig. 5(b)) are too small to be visible atop the symbols. This indicates that Eq. (B3) with scaling parameter δ is an excellent analytical approximation for the scaling function $\tilde{f}$.

Additionally, we observe that the normalized values of δ given by $\delta(n)/\delta(n=2)$ exactly overlaps on top of each other. This indicates that the value of $\delta = \delta^{geom}.\delta^{n}$, where δ^{geom} is a constant entirely dependent on the geometrical support configuration, and δ^{n} is a constant dependent on the electrostatic dimension of the system.

APPENDIX C: κ in C_{bp}-V RELATIONSHIP FOR CIRCULAR ELECTRODES

For the post pull-in state, the value of C_{pp} is approximated in terms of the total electrode area (A), contacted area (A_c), and non-contact area (A_a) (Eq. (A6)), to eventually obtain

$$\frac{C_{ON} - C_{PO}}{C_{ON} - C_{pp}} = \frac{A}{A_a}. \tag{C1}$$

In the case of a circular membrane, $\frac{A}{A_a} = \frac{R^2}{R^2 - r^2}$, where R is the radius of the top electrode and r is the radius of the region in contact with the bottom electrode. Using the terminology in Eq. (A6), $L \equiv R$ and $l \equiv (R - r)$, Eq. (C1) can be written as follows:

$$\frac{C_{ON} - C_{PO}}{C_{ON} - C_{pp}} = \frac{R^2}{R^2 - r^2} = \frac{L^2}{L^2 - (L-l)^2} = \frac{L^2}{l^2\left(\frac{2L}{l} - 1\right)} \approx \frac{L}{2l} \approx \left(\frac{V}{V_{PO}}\right)^{\frac{1}{2}}. \tag{C2}$$

Hence, the value of $\kappa \approx 0.5$ is justified, even in the case of a circular membrane. A similar argument can be applied for cross-shaped electrodes as well. Apart from the approximation used in Eq. (A6), the approximation in Eq. (C2) also contributes to the small spread observed in the values of κ (around the value of 0.5) in numerical simulations for circular and cross-shaped electrode support configurations.

[1]J. J. Yao, J. Micromech. Microeng. **10**, R9–R38 (2000).
[2]P. F. Van Kessel, L. J. Hornbeck, R. E. Meier, and M. R. Douglass, Proc. IEEE **86**, 1687–1704 (1998).
[3]A. Q. Liu and X. M. Zhang, J. Micromech. Microeng. **17**, R1 (2007).
[4]A. Q. Liu, B. Zhao, F. Chollet, Q. Zou, A. Asundi, and H. Fujita, Sens. Actuators, A **86**, 127–134 (2000).
[5]T. G. Bifano, J. Perreault, R. Krishnamoorthy Mali, and M. N. Horenstein, IEEE J. Sel. Top. Quantum. Electron. **5**, 83–89 (1999).
[6]D. Peroulis, S. P. Pacheco, K. Sarabandi, and L. P. B. Katehi, IEEE Trans. Microwave Theory Tech. **51**, 259–270 (2003).
[7]C. Goldsmith, T.-H. Lin, B. Powers, W.-R. Wu, and B. Norvell, IEEE MTT-S Int. Microwave Symp. Dig. **1**, 91–94 (1995).
[8]S. Majumder, J. Lampen, R. Morrison, and J. Maciel, IEEE MTT-S Int. Microwave Symp. Dig. **3**, 1935–1938 (2003).
[9]K. Akarvardar and H.-S. P. Wong, IEEE Electron Device Lett. **30**, 1143–1145 (2009).
[10]B. Gally, A. Lewis, K. Aflatooni, W. Cummings, S. Ganti, M. Todorovich, and R. van Lier, SID Int. Symp. Digest Tech. Papers **42**, 36–39 (2011).
[11]M. I. Younis, E. M. Abdel-Rahman, and A. Nayfeh, J. Microelectromech. Syst. **12**, 672–680 (2003).
[12]E. M. Abdel-Rahman, M. I. Younis, and A. H. Nayfeh, J. Micromech. Microeng. **12**, 759 (2002).
[13]G. Taylor, Proc. R. Soc. London, Ser. A **280**, 383–397 (1964).
[14]H. C. Nathanson, W. E. Newell, R. A. Wickstrom, and J. R. Davis, IEEE Trans. Electron Devices **14**, 117–133 (1967).
[15]C. Chen, K. I. Bolotin, W. Kalb, P. Kim, I. Kymissis, H. L. Stormer, T. F. Heinz, and J. Hone, Nat. Nanotechnol. **4**, 861–867 (2009).
[16]M. Dequesnes, S. V. Rotkin, and N. R. Aluru, Nanotechnology **13**, 120 (2002).
[17]X. L. Feng, R. He, P. Yang, and M. L. Roukes, Nano Lett. **7**, 1953–1959 (2007).
[18]A. San Paulo, N. Arellano, J. A. Plaza, R. He, C. Carraro, R. Maboudian, R. T. Howe, J. Bokor, and P. Yang, Nano Lett. **7**, 1100–1104 (2007).
[19]Y. Mafinejad, A. Z. Kouzani, K. Mafinezhad, and H. Nabovatti, IEEE Trans. Syst. Man Cybern. **2009**, 4623–4627.
[20]C. L. Goldsmith, D. I. Forehand, Z. Peng, J. C. M. Hwang, and J. L. Ebel, IEEE MTT-S Int. Microwave Symp. Dig. **2007**, 1805–1808.
[21]A. Jain, P. R. Nair, and M. A. Alam, Appl. Phys. Lett. **98**, 234104 (2011).
[22]E. K. Chan, E. C. Kan, R. W. Dutton, and P. M. Pinsky, IEEE MTT-S Int. Microwave Symp. Dig. **3**, 1511–1514 (1997).
[23]R. Lefèvre, M. F. Goffman, V. Derycke, C. Miko, L. Forró, J. P. Bourgoin, and P. Hesto, Phys. Rev. Lett. **95**, 185504 (2005).
[24]L. X. Zhang and Y.-P. Zhao, Microsyst. Technol. **9**, 420–426 (2003).
[25]S. Pamidighantam, R. Puers, K. Baert, and H. A. C. Tilmans, J. Micromech. Microeng. **12**, 458–464 (2002).
[26]S. Li and S. Chen, Sens. Actuators, A **104**, 151–161 (2003).
[27]G. M. Rebeiz, *RF MEMS: Theory, Design, and Technology* (John Wiley & Sons, Inc., 2004).

[28]W. M. van Spengen, Microelectron. Reliab. **43**, 1049–1060 (2003).
[29]A. Jain, S. Palit, and M. A. Alam, J. Microelectromech. Syst. **21**, 420–430 (2012).
[30]S. Palit and M. A. Alam, J. Appl. Phys. **111**, 054112 (2012).
[31]M. Koutsoureli, N. Tavassolian, G. Papaioannou, and J. Papapolymerou, Appl. Phys. Lett. **98**, 093505-3 (2011).
[32]See www.radantmems.com for cantilever based radio frequency ohmic switches.
[33]Y. Ozaki, T. Ohyama, T. Yasuda, and I. Shimoyama, in *IEEE International Conference on Micro Electro Mechanical Systems* (MEMS) (2000), pp. 531–536.
[34]W. H. Ko, M.-H. Bao, and Y.-D. Hong, IEEE Trans. Electron. Devices **29**, 48–56 (1982).
[35]H. Samavati, A. Hajimiri, A. R. Shahani, G. N. Nasserbakht, and T. H. Lee, IEEE J. Solid-State Circuits **33**, 2035–2041 (1998).
[36]See supplementary material at http://dx.doi.org/10.1063/1.4798365 for detailed description of numerical simulations and method of moments used for the calculation of electrostatic force.
[37]A. E. H. Love, Philos. Trans. R. Soc. London, Ser. A **179**, 491–546 (1888).
[38]B. Y. Park, R. Zaouk, C. Wang, and M. J. Madou, J. Electrochem. Soc. **154**, P1–P5 (2007).
[39]C. Puente-Baliarda, J. Romeu, R. Pous, and A. Cardama, IEEE Trans. Antennas Propag. **46**, 517–524 (1998).
[40]K. B. Lee, Sens. Actuators, A **133**, 518–525 (2007).
[41]S. Gorthi, A. Mohanty, and A. Chatterjee, J. Micromech. Microeng. **16**, 1800 (2006).